

# Complex free-space magnetic field textures induced by 3D magnetic nanostructures

## Author List:

Claire Donnelly<sup>1,2\*</sup>, Aurelio Hierro-Rodríguez<sup>3,4,5</sup>, Claas Abert<sup>6</sup>, Katharina Witte<sup>7,8</sup>, Luka Skoric<sup>1</sup>, Dédalo Sanz-Hernández<sup>1</sup>, Simone Finizio<sup>7</sup>, Fanfan Meng<sup>1</sup>, Stephen McVitie<sup>3</sup>, Jörg Raabe<sup>7</sup>, Dieter Suess<sup>6</sup>, Russell Cowburn<sup>1</sup>, Amalio Fernández-Pacheco<sup>9\*</sup>

## Affiliations:

<sup>1</sup> Cavendish Laboratory, University of Cambridge, JJ Thomson Ave, Cambridge, CB3 0HE, UK.

<sup>2</sup> Max Planck Institute for Chemical Physics of Solids, 01187 Dresden, Germany.

<sup>3</sup> SUPA, School of Physics and Astronomy, University of Glasgow, Glasgow G12 8QQ, UK.

<sup>4</sup> Departamento de Física, Universidad de Oviedo, 33007 Oviedo, Spain.

<sup>5</sup> CINN (CSIC-Universidad de Oviedo), 33940 El Entrego, Spain.

<sup>6</sup> Faculty of Physics, University of Vienna, 1090 Vienna, Austria.

<sup>7</sup> Swiss Light Source, Paul Scherrer Institute, 5232 Villigen, Switzerland.

<sup>8</sup> Berlin Partner für Wirtschaft und Technologie GmbH, 10623 Berlin, Germany

<sup>9</sup> Instituto de Nanociencia y Materiales de Aragón, 50009 Zaragoza, Spain.

\*Correspondence to: [claire.donnelly@cpfs.mpg.de](mailto:claire.donnelly@cpfs.mpg.de), [amaliofp@unizar.es](mailto:amaliofp@unizar.es)

## Introductory paragraph:

The design of complex, competing effects in magnetic systems – be it via the introduction of nonlinear interactions [1, 2], or the patterning of three-dimensional geometries [3] – is an emerging route to achieve new functionalities. In particular, through the design of 3D geometries and curvature, intra-structure properties such as anisotropy and chirality, both geometry-induced and intrinsic, can be directly controlled, leading to a host of new physics and functionalities, such as 3D chiral spin states [4], ultra-fast chiral domain wall dynamics [5-7] and spin textures with new spin topologies [4, 8]. Here, we advance beyond the control of intra-structure properties in 3D and tailor the magnetostatic coupling of neighbouring magnetic structures – an *inter-structure* property – which allows us to generate complex textures in the magnetic stray field. For this, we harness direct write nanofabrication techniques, creating intertwined nanomagnetic cobalt double helices, where curvature, torsion, chirality, and magnetic coupling are jointly exploited. By reconstructing the 3D vectorial magnetic state of the double helices with soft X-ray magnetic laminography [9, 10], we identify the presence of a regular array of highly coupled *locked* domain wall pairs in neighbouring helices. Micromagnetic simulations reveal that the magnetisation configuration leads to the formation of an array of complex textures in the magnetic *induction*, consisting of vortices in the magnetisation and antivortices in free space, which

together, form an effective B-field cross-tie wall [11]. The design and creation of complex three-dimensional magnetic field nanotextures opens new possibilities for smart materials [12], unconventional computing [2, 13, 14], particle trapping [13, 15] and magnetic imaging [16].

### Main Text:

We consider a model system that consists of two intertwined, yet spatially separated, ferromagnetic nanohelices. This three-dimensional nanomagnetic system has a complex energy landscape defined by the balance of competing intra- and inter-helix effects (terms defined above). The nanoscale double helix combines effects of curvature and torsion that may result in curvature-induced magnetic anisotropy and chirality effects [20-22]. Specifically, the two helices are designed to have the same chirality, and are offset by half a period, leading to a constant inter-helix separation along the length of the system. We fabricate the system of two intertwined cobalt nanohelices with focused electron beam induced deposition [23]. Scanning electron microscope (SEM) images of two nano double helices are presented in **Figure 1**, the first (Double Helix A, **Figure 1c**) with lower pitch and higher radius, the second (Double Helix B, **Figure 1d**) more elongated with higher pitch and lower radius (geometries defined in **Table 1**). Both double helices have a nanowire diameter of approximately 70-80 nm with an inter-helix distance of ~50-70 nm and therefore exhibit significant magnetostatic coupling.

To probe the magnetic state of these complex three-dimensional magnetic nanostructures, we employ scanning transmission X-ray microscopy (STXM, **Figure 1e**). By tuning the X-ray energy to the Co  $L_2$  edge (796 eV) and measuring images with circular polarisation, we exploit X-ray magnetic circular dichroism (XMCD) to obtain a high spatial resolution projection of the magnetisation parallel to the X-ray beam (**Figure 1f**). We first probe the as-grown state of the two magnetic double helices in **Figure 1f,g**, where one can see that in both XMCD images, the double helices are composed of a dark and a bright helix, which corresponds to the individual helices being in antiparallel-magnetised single domain states with a quasi-tangential magnetisation distribution. This is expected due to the radii of curvature and torsion (defined in Table 1) being significantly larger than both the exchange length (4-6 nm) and the diameter of the nanowires [20]. These two antiparallel double helix states (magnetisation of Helix A and B either positive and negative or negative and positive, respectively) represent the degenerate ground states of the system (see **Methods**), and result due to the fabrication sequence of the helices, which are grown in parallel: at the start of the growth when the helices are small, the magnetic moments reorient to minimise the magnetostatic energy, aligning antiparallel to one another. This antiparallel state is maintained as the helices are grown, leading to the formation of these single domain, micrometre-length structures [4].

Although the two double helix systems form a similar antiparallel state in their as-grown configuration, they exhibit very different behaviours under the application of a magnetic field perpendicular to the long axis of the helix. The XMCD projection of Double Helix A again reveals a pair of dark and bright helices, indicating the return to an antiparallel state (specifically the opposite antiparallel state, **Figure 1h**). However, the XMCD projection of Double Helix B is different, with alternating regions of dark and bright contrast within individual helices (**Figure 1i**) indicating the formation of a multidomain state with a regular array of domain walls. With both double helix systems composed of the same material and exposed to the same external magnetic field, we attribute this difference in behaviour to their different curvature, torsion, and inter-helix coupling.

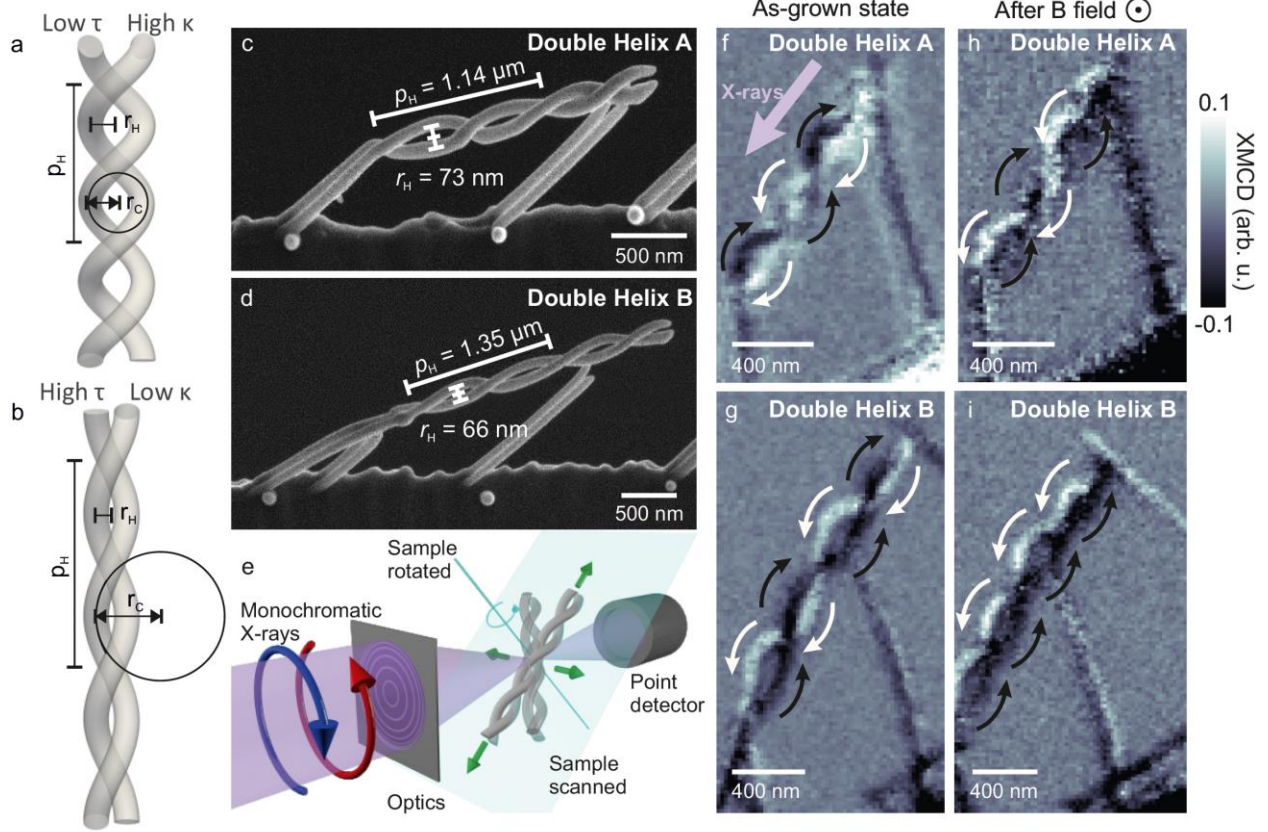


**Figure 1. Ferromagnetic double helices.** *a,b* the pitch  $p_H$  and radius  $r_H$  of the helix determine the radius of curvature  $r_c = 1/\kappa$ , and the torsion  $\tau$  of the system. *c,d* Ferromagnetic double helix nanostructures, with varying helix pitch,  $p_H$ , and radius,  $r_H$ , ( $2r_H$  indicated) and a nanowire diameter of  $\sim 70$ - $80$  nm. Additional straight cobalt pillars are included to sustain the nanostructure and facilitate the X-ray microscopy experiments. *e* The magnetic state is probed using STXM and XMCD using a laminography setup for 3D imaging, providing nanoscale projections of the magnetisation parallel to the X-ray direction (indicated by purple arrow in *f*). *f,g* In the as-grown state both double helices are composed of two fully black and white helices – corresponding to antiparallel magnetised single domain helices. *h,i* After the application of a saturating field transverse to the helix long axis, Double Helix A returns to the antiparallel state (*h*), while Double Helix B remains in a multi-domain state identified by alternating bright and dark regions within the individual helices (*i*). Black and white arrows indicate the direction of the magnetisation in each image.

To elucidate the influence of the three-dimensional geometry on the remanent magnetic configuration, we simulate the magnetic configuration formed after the application of a saturating transverse magnetic field for a variety of helix pitches and radii using finite-element micromagnetic simulations [24]. We identify three remanent magnetic configurations: first, the antiparallel state (**Figure 2ai**), as observed experimentally for Double Helix A (**Figure 1f**). Second, an unlocked domain wall state (**Figure 2aii**) in which the transverse domain walls are aligned in the direction of the applied magnetic field. This unidirectional state is characterised by having the net magnetic surface charge of the walls located at the outer curved section of the wires, as favoured by the curvature-induced anisotropy and the curvature-induced Dzyaloshinskii-Moriya Interaction (DMI), which promote a particular domain wall chirality [25]. This state is consistent with the equivalent magnetic configurations of planar magnetic nanowires [25, 26]. For geometries that host the unlocked state at remanence, the curvature-induced effects dominate over the inter-structure magnetostatic interaction. We also observe a third, unconventional domain wall configuration (**Figure 2aiii**) in which the domain walls fully *reverse* with respect to both the direction of the applied magnetic field and the curvature-induced DMI, becoming locked in place due to the strong inter-helix interaction, as shown schematically in **Figure 2b**.

To determine whether the locked domain wall state is present in Double Helix B, we perform soft X-ray magnetic laminography [9, 10, 27] [28] (**Figure 1e**) to map its three-dimensional magnetisation vector field

with nanoscale resolution. The reconstructed magnetisation is given by arrows in **Figure 2d**, where a reversal of the direction of the magnetisation within the magnetic domain walls can be observed, consistent with the locked domain wall state. An additional representation of the magnetisation with streamlines (**Figure 2e**) reveals a distinctive figure-of-8 structure in the reconstructed magnetisation. When compared with micromagnetic simulations in **Figure 2f,g** (see also **Extended Data 1**), the figure-of-8 structure is reproduced, providing confirmation of the reversal of the domain wall direction and the resulting locked domain wall array in Double Helix B.

The formation of these different remanent states – the antiparallel state and locked domain wall state for Double Helices A and B, respectively – occurs due to the geometry of the double helices strongly affecting the competing interactions. Specifically, the higher torsion:curvature ratio of Double Helix B, associated with its higher helix pitch and lower helix radius, promotes the formation of a stable array of locked domain walls. After the formation of the unlocked domain walls following transverse saturation, the domain walls reorient due to the magnetostatic interaction overcoming the curvature-induced DMI of the domain wall. In particular, the higher torsion:curvature ratio decreases the distance between the helices, increasing the magnetostatic interaction between them, while at the same time decreasing the curvature-induced DMI, promoting the rotation of the domain walls to the locked state (See **Methods**). This reorientation creates a more confined magnetic flux, reducing the magnetostatic energy, as shown schematically in **Figure 2b**. In contrast, the antiparallel state observed in Double Helix A forms due to the higher curvature and lower torsion. Specifically, as the inter-domain wall distance in different helices increases, the coupling between domain walls in *different* helices decreases, and the distance between domain walls *within* a single helix is reduced. Both effects favour the annihilation of neighbouring domain wall pairs and the formation of the antiparallel state. This geometry-dependent behaviour in intertwined double-helices is confirmed by both mapping the phase diagram of this system with micromagnetic simulations and an analytical model (see **Methods** and **Supporting Information Sections I and II**) confirming that the locked domain wall state forms as a result of the influence of the geometry on these competing effects.

The locked domain wall state observed here occurs due to the balance between intra-helix properties, and inter-helix coupling. While it is known that curvature and torsion influence intra-nanowire properties such as anisotropies and chirality [19-22, 30], their influence on inter-nanostructure coupling – *i.e.* the magnetic stray field generated by neighbouring 3D structures – remains unexplored. To elucidate the influence of the three-dimensional geometry on the magnetostatic coupling, we calculate the magnetic induction  $\mathbf{B} = \mu_0(\mathbf{H} + \mathbf{M})$  in the whole space (including both the magnetic material and free space) by taking the magnetisation configuration  $\mathbf{M}$  of the locked domain wall state from micromagnetic simulations and computing its stray field ( $\mathbf{H}$ ). We first consider the overall structure of  $\mathbf{B}$  within the helix: the formation of the regular array of domain walls results in the double helix being split into two main domains, as shown in **Figure 3a**, where on the left, the magnetisation points down along  $-\hat{x}$  (blue) and on the right, the magnetisation points up along  $+\hat{x}$  (red). This asymmetry in  $\mathbf{B}$  within the double helix results in a similar asymmetry in  $\mathbf{B}$  in free space, seen by considering the variation in the stray field surrounding the domain walls. While the highest stray fields in free space ( $\mathbf{B} = \mu_0\mathbf{H} > 0.3\mu_0M_s$ ) are found to mostly align horizontally ( $\hat{y}$ ) between the domain wall pairs (left panel of **Figure 3b**), as lower magnitude stray fields are considered (middle and right panels of **Figure 3b**), we observe a growing component of the stray field in the plane of the domain wall cross section (x-z plane), that becomes more noticeable when weaker stray fields  $> 0.1|M_s|$  are plotted. In fact, the stray field is seen to *rotate asymmetrically* into the x-z plane to channel the magnetic flux of magnetic domains of the same direction in the two different helices (**Figure 3c**): on one side, the stray field develops a (blue) negative vertical  $\hat{x}$  component to channel the flux of the (blue) negative  $m_x$  domains, while on the other side, the stray field tilts into the (red) positive  $\hat{x}$  direction to connect domains of (red) positive  $m_x$ , indicated by blue and red arrows in **Figure 3c**.

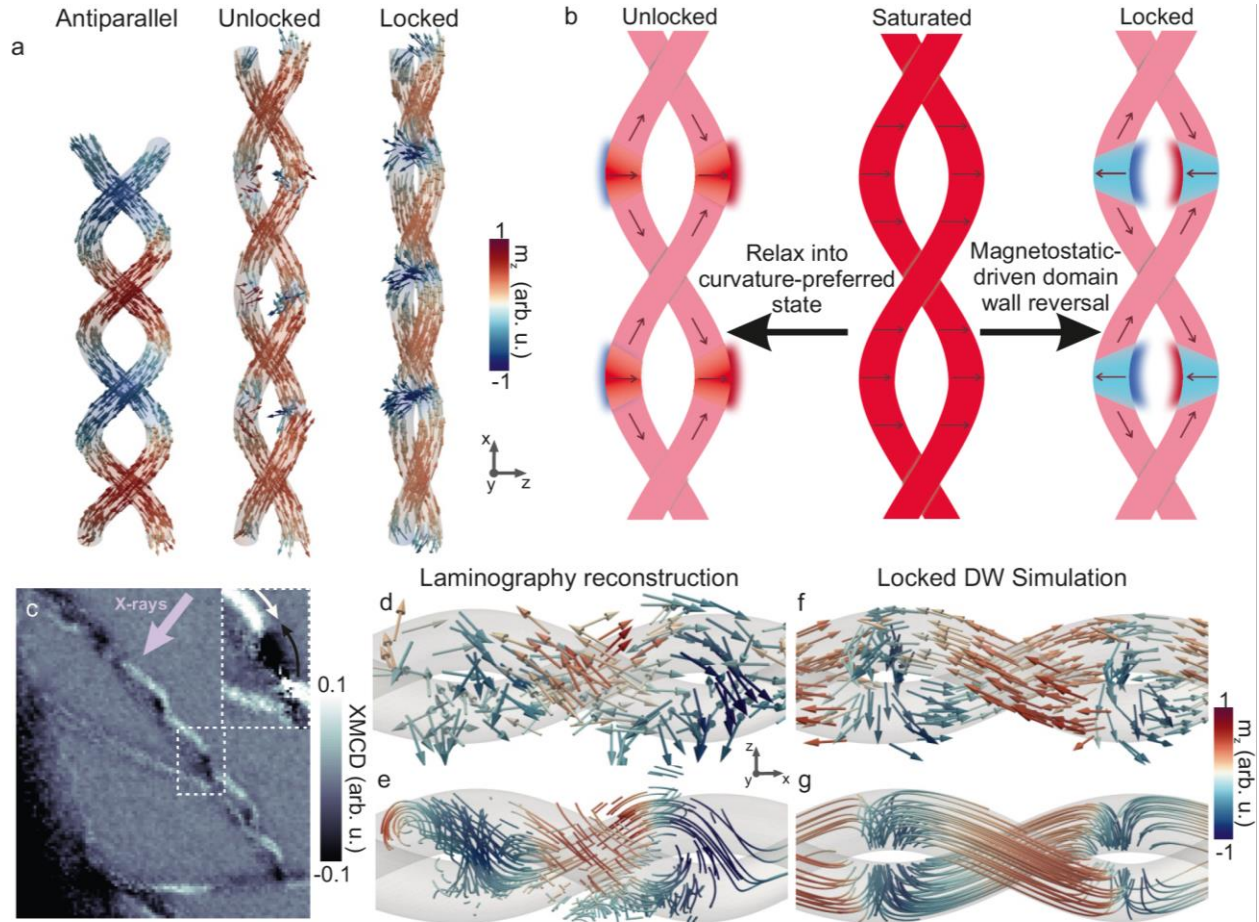


Figure 2. The “locked” domain wall state. a) Finite element micromagnetic simulations of double helices with varying pitch and radii reveal three stable configurations after the presence of a transverse saturating magnetic field: the antiparallel state, as well as regularly spaced unlocked and locked domain wall pairs. b) When the locked state is the stable remanent state, the saturated state relaxes to the unlocked domain wall state, before the domain wall pairs reorient due to the magnetostatic interaction to form the locked state. c) An XMCD projection of Double Helix B rotated by  $60^\circ$  from Figure 1 reveals a periodic array of domain walls (with the position of one domain wall revealed by the transition from black to white and indicated by arrows shown in inset). X-ray direction indicated by purple arrow. d-e) Soft X-ray laminography reveals the 3D structure of the domain walls, with the reconstructed magnetisation represented by d) arrows and e) streamlines, revealing a figure-of-8 texture. f-g) The presence of the locked domain wall state is confirmed by comparison with micromagnetic simulations of the “locked” domain wall state (f), with streamlines indicating the direction of the magnetisation (g) again revealing the recognisable “figure-of-8” texture in the magnetisation that indicates the reversal of the domain walls.

The formation of these asymmetric magnetic flux channels not only results in a deviation from the direct horizontal coupling of the domain walls but induces a distinctive asymmetric structure into the magnetic induction itself. Indeed, when the magnetic induction is projected onto the x-z plane perpendicular to the direction of the domain walls (indicated in **Figure 4a**) the asymmetric  $\hat{x}$  components of the induction caused by the flux channels result in the formation of a saddle-like structure surrounding the domain wall pair that resembles an antivortex quadrupole structure [31] (**Figure 4b**). We confirm the presence of antivortices in the magnetic induction by calculating the winding number of the normalised components of the induction in the x-z plane to be -1. These textures are not only of interest for their topological nature, but also for the type of magnetic forces that could be generated. Indeed, the non-trivial in-plane structure exhibit well-defined gradients in the x-z plane components of the magnetic field, offering a new route to the design of nanoscale gradients in the magnetic induction.

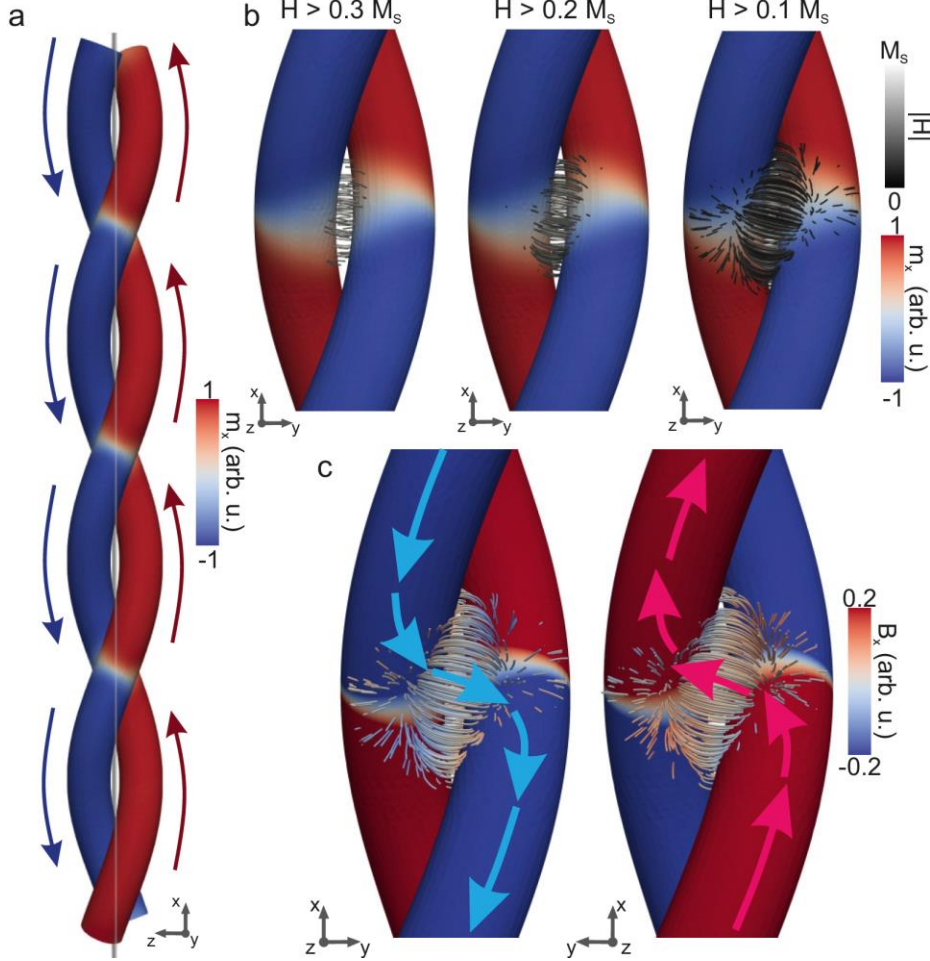
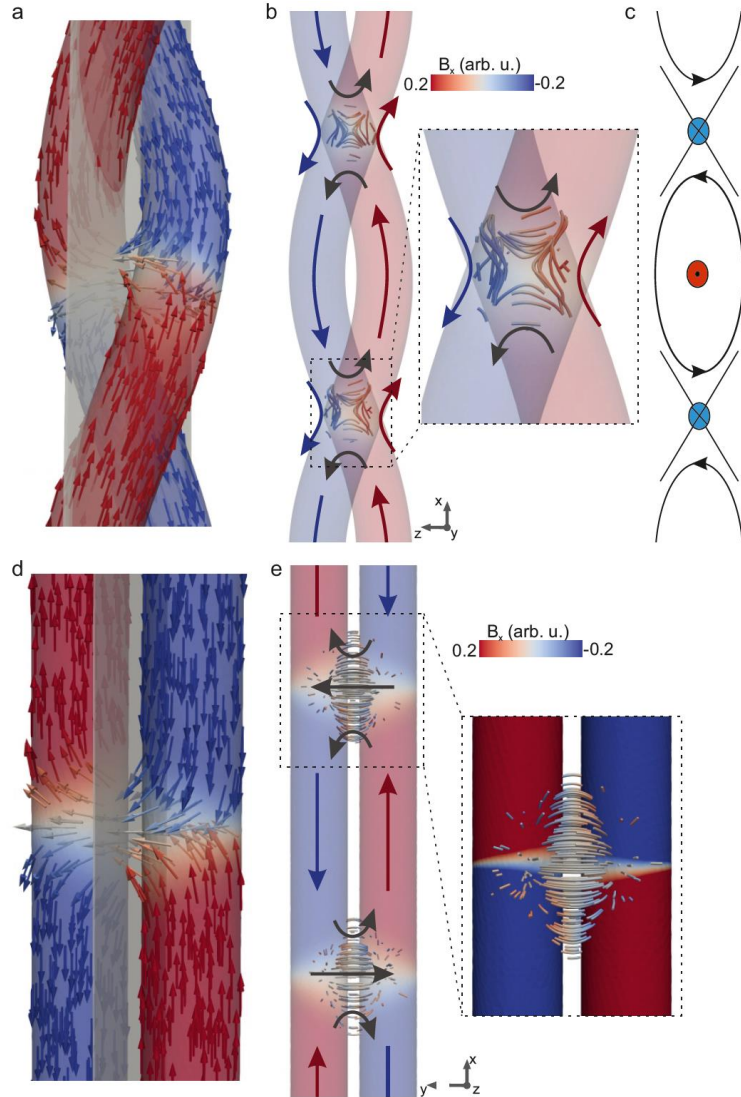


Figure 3 Flux channelling in the locked domain wall state. a) the array of domain walls leads to the double helix being split into negative (left, blue) and positive (right, red)  $m_x$  domains. b) The stray field  $H$  of a locked domain wall pair is plotted, with its magnitude indicated by the black-white colour scale, indicating that while the strongest fields ( $H > 0.3|H_{max}|$ ) align horizontally between domain walls, weaker, but still significant, components of the stray field ( $H > 0.2|H_{max}|$  and  $H > 0.1|H_{max}|$ ) rotate into the  $x$  direction, forming a “flux channel” between magnetic domains of the same axial direction. c) This flux channel is confirmed by plotting the direction of the stray field with the magnetization on either side of the double helix, where the stray field connects magnetic domains of the same direction, but in different helices (indicated by blue and red arrows).

Due to the periodic geometry of the double helix, the in-plane antivortices are not isolated objects: the regular array of locked domain walls leads to an array of effective antivortices in the magnetic stray field (**Figure 4b**). In addition, the magnetisation configuration of the locked domain wall state in the chiral double helix forms an array of vortices of constant chirality in  $\mathbf{B}$  (with winding number +1), that is defined by the chiral geometry. The combination of the alternating chiral vortices and antivortices in  $\mathbf{B}$  is reminiscent of the cross-tie wall in planar magnetic elements [11, 32] (**Figure 4c**), where the continuity of the magnetisation requires the presence of a crossing of the magnetisation between like-handed vortices [33]. Here, we observe this contained *effective cross-tie B-field domain wall*-like structure composed of vortices in the magnetisation and antivortices in the  $\mathbf{B}$  field in free space.

To confirm the role of the chirality of the helix in the formation of these complex  $\mathbf{B}$  field textures, we consider the equivalent domain wall configuration in a non-helical, *achiral* geometry composed of straight nanowires. To remove the helical geometry, we perform additional simulations after applying a coordinate transformation to the locked domain configuration, effectively unwinding the helices to a pair of straight nanowires (see **Methods**) and removing the influence of the three-dimensional chiral geometry of the helices, and the associated curvilinear effects. Following the relaxation of the magnetisation from the locked

state under this new geometry (**Figure 4d**), we observe no vertical component of the stray field coupling domains of the same direction in different nanowires (**Figure 4e**), indicating that no flux channelling (as observed in the double helix, **Figure 3c**) occurs. Due to the absence of flux channelling, no antivortex textures are observed in the stray field, confirming that the stray field textures observed surrounding the locked domain wall state are a direct consequence of the twisting of the chiral helix structure.



*Figure 4. Textures in the  $\mathbf{B}$  field of the locked domain wall state. Plotting the induction in the  $x$ - $z$  plane (plane indicated with respect to magnetic configuration in a), an array of antivortices in the in-plane components of the  $\mathbf{B}$  field, plotted with streamlines, is observed (b), in between effective vortices formed by the chiral magnetisation. The structure of the antivortex is shown in greater detail in the inset. Schematic arrows are added to show the direction of  $\mathbf{B}$ . (c) The array of vortices and antivortices resembles the structure of a cross-tie domain wall. (d-e) These textures in the stray field do not occur in the corresponding configuration of straight cylindrical nanowires where (e) the stray field ( $H > 0.1|H_{\max}|$ ) exhibits no flux channelling (see inset) and there are no antivortices present in the magnetic induction.*

We have demonstrated that the three-dimensional geometry cannot only alter intra-structure properties, but also offers an opportunity to tailor the magnetic field itself. This is showcased in our double helix system where the three-dimensional geometry results in highly stable and robust *locked* domain wall pairs, with prospects for robust domain wall motion and synchronous dynamics [34, 35] in 3D interconnectors, key to the realisation of spin logic in large scale integrated 3D circuits. These phenomena are of great interest for domain wall conduit-based information processing [36], which includes emerging applications such as

reservoir computing [2, 37] where the strong interaction between neighbouring magnetic textures and the controlled reconfigurability that these systems present, is of key importance. In particular, the introduction of non-linear interactions into a system provides the opportunity for the combination of both information transmission and processing, and the possibility to go beyond von Neumann computing architectures. Moreover, the creation of an array of planar antivortices in the magnetic field in free space sets a precedent for the creation of topological magnetic field textures with complex nanoscale field gradients using 3D magnetic nanostructures. The design of controlled gradients in the magnetic field is key for applications such as particle [15] and cold-atom [13] trapping, while the ability to define complex nanotextures in the magnetic field has significant implications for imaging [38, 39] and magnetic field manipulation [40]. While emergent topological features in the magnetic stray field have previously been found to result in chiral behaviour in frustrated nanomagnet arrays [41], here 3D nano-patterning results in the *controlled* creation of well-localised magnetic field antivortices. These results demonstrate that the properties of a three-dimensional system can not only be used to tailor the material internal spin states but play a key role in defining the magnetic stray field, and thus the interaction of neighbouring features in the magnetisation.

### **Acknowledgments:**

All data was measured at the PoLux beamline, Swiss Light Source, Paul Scherrer Institute, Switzerland. Samples were grown in the MCMP Group in the School of Physics, University of Glasgow. This work was funded by an EPSRC Early Career Fellowship EP/M008517/1 and the Winton Program for the Physics of Sustainability. C.D. acknowledges funding from the Leverhulme Trust (ECF-2018-016), the Isaac Newton Trust (18-08), the L'Oréal-UNESCO UK and Ireland Fellowship For Women In Science 2019, and the Max Planck Society Lise Meitner Excellence Program. A.F.P. acknowledges funding by the European Community under the Horizon 2020 Program, Contract no. 101001290, 3DNANOMAG. A.H.-R. and S.M.V. acknowledge the support from European Union's Horizon 2020 research and innovation program under Marie Skłodowska-Curie grant ref. H2020-MSCA-IF-2016-746958. A.H.-R. acknowledges funding from Spanish AEI under project reference PID2019-104604RB/AEI/10.13039/501100011033. The PoLux end station was financed by the German Ministerium für Bildung und Forschung (BMBF) through contracts 05K16WED and 05K19WE2. K.W. acknowledges the funding from the European Union's Horizon 2020 research and innovation program under the Marie Skłodowska-Curie grant agreement no. 701647. A.F.P. is grateful to the University of Cambridge and the University of Glasgow, where part of this research was performed. The authors thank Sam McFadzean, William Smith and Colin How for their support with sample fabrication, and Paul Sutcliffe for fruitful discussions.

### **Author contributions:**

CD, AHR, DSH, AFP conceived the project. The samples were fabricated by CD with the support of AHR, LS and AFP. The synchrotron measurements were performed by CD, AHR, KW, SF, FM, AFP, and data analysis performed by CD, AHR, KW, DSH and AFP. The 3D magnetic reconstruction was developed and implemented by CD, and the results interpreted by CD, AHR and AFP. Micromagnetic simulations were performed by CD, AHR and CA with the support of DS. All authors contributed to the interpretation of the results and the writing of the manuscript.

### **Competing interests:**

Authors declare no competing interests.

### **Tables:**

	Nanowire diameter	Helix radius	Helix pitch	Radius of curvature, $\kappa^{-1}$	Radius of torsion, $\tau^{-1}$
<b>Helix A</b>	70 nm	73 nm	1.14 $\mu\text{m}$	523 nm	210 nm
<b>Helix B</b>	70 nm	66 nm	1.35 $\mu\text{m}$	765 nm	235 nm

Table 1. Parameters of the three-dimensional geometries of the two nanoscale double helices investigated in this work, and shown in Figure 1a,b.

## References:

- Romera, M., et al., *Vowel recognition with four coupled spin-torque nano-oscillators*. Nature, 2018. **563**(7730): p. 230-234.
- Grollier, J., et al., *Neuromorphic spintronics*. Nature Electronics, 2020. **3**(7): p. 360-370.
- Fernández-Pacheco, A., et al., *Three-dimensional nanomagnetism*. Nature Communications, 2017. **8**: p. 15756.
- Sanz-Hernández, D., et al., *Artificial Double-Helix for Geometrical Control of Magnetic Chirality*. ACS Nano, 2020. **14**(7): p. 8084-8092.
- Yan, M., et al., *Chiral symmetry breaking and pair-creation mediated Walker breakdown in magnetic nanotubes*. Applied Physics Letters, 2012. **100**(25): p. 252401.
- Hertel, R., *Curvature-induced magnetochirality*. Spin, 2013. **3**(3): p. 1340009 (9 pp.)-1340009 (9 pp.).
- Hertel, R., *Ultrafast domain wall dynamics in magnetic nanotubes and nanowires*. J. Phys.: Cond. Matt., 2016. **28**(48): p. 483002.
- Da Col, S., et al., *Observation of Bloch-point domain walls in cylindrical magnetic nanowires*. Physical Review B, 2014. **89**(18): p. 180405.
- Donnelly, C., et al., *Time-resolved imaging of three-dimensional nanoscale magnetization dynamics*. Nature Nanotechnology, 2020. **15**(5): p. 356-360.
- Witte, K., et al., *From 2D STXM to 3D Imaging: Soft X-ray Laminography of Thin Specimens*. Nano Letters, 2020. **20**(2): p. 1305-1314.
- Metlov, K.L., *Cross-Tie Domain Wall Ground State in Thin Films*. Journal of Low Temperature Physics, 2005. **139**(1): p. 207-219.
- Li, Z., F. Yang, and Y. Yin, *Smart Materials by Nanoscale Magnetic Assembly*. Advanced Functional Materials, 2020. **30**(2): p. 1903467.
- Romero-Isart, O., et al., *Superconducting Vortex Lattices for Ultracold Atoms*. Physical Review Letters, 2013. **111**(14): p. 145304.
- Bhanja, S., et al., *Non-Boolean computing with nanomagnets for computer vision applications*. Nature Nanotechnology, 2016. **11**(2): p. 177-183.
- Cao, Q., et al., *Recent advances in manipulation of micro- and nano-objects with magnetic fields at small scales*. Materials Horizons, 2020. **7**(3): p. 638-666.
- Corte-León, H., et al., *Magnetic bead detection using domain wall-based nanosensor*. J. Appl. Phys., 2015. **117**(17): p. 17E313.
- Skjærvø, S.H., et al., *Advances in artificial spin ice*. Nature Reviews Physics, 2020. **2**(1): p. 13-28.
- Lehmann, J., et al., *Poling of an artificial magneto-toroidal crystal*. Nature Nanotechnology, 2019. **14**(2): p. 141-144.
- Streubel, R., et al., *Magnetism in curved geometries*. Journal of Physics D: Applied Physics, 2016. **49**(36): p. 363001.
- Sheka, D.D., et al., *Torsion-induced effects in magnetic nanowires*. Physical Review B, 2015. **92**(5): p. 054417.
- Denis, D.S., P.K. Volodymyr, and G. Yuri, *Curvature effects in statics and dynamics of low dimensional magnets*. Journal of Physics A: Mathematical and Theoretical, 2015. **48**(12): p. 125202.
- Gaididei, Y., V.P. Kravchuk, and D.D. Sheka, *Curvature Effects in Thin Magnetic Shells*. Physical Review Letters, 2014. **112**(25): p. 257203.
- Skoric, L., et al., *Layer-by-Layer Growth of Complex-Shaped Three-Dimensional Nanostructures with Focused Electron Beams*. Nano Letters, 2020. **20**(1): p. 184-191.
- Abert, C., et al., *magnum.fe: A micromagnetic finite-element simulation code based on FEniCS*. Journal of Magnetism and Magnetic Materials, 2013. **345**: p. 29-35.

25. Volkov, O.M., et al., *Experimental Observation of Exchange-Driven Chiral Effects in Curvilinear Magnetism*. Physical Review Letters, 2019. **123**(7): p. 077201.
26. Lewis, E.R., et al., *Magnetic domain wall pinning by a curved conduit*. Applied Physics Letters, 2009. **95**(15): p. 152505.
27. Donnelly, C., et al., *Three-dimensional magnetization structures revealed with X-ray vector nanotomography*. Nature, 2017. **547**: p. 328.
28. Donnelly, C., et al., *Tomographic reconstruction of a three-dimensional magnetization vector field*. New Journal of Physics, 2018. **20**(8): p. 083009.
29. O'Brien, L., et al., *Near-Field Interaction between Domain Walls in Adjacent Permalloy Nanowires*. Physical Review Letters, 2009. **103**(7): p. 077206.
30. Yershov, K.V., et al., *Geometry-induced motion of magnetic domain walls in curved nanostripes*. Physical Review B, 2018. **98**(6): p. 060409.
31. Gliga, S., R. Hertel, and C.M. Schneider, *Switching a magnetic antivortex core with ultrashort field pulses*. Journal of Applied Physics, 2008. **103**(7): p. 07B115.
32. Huber, E.E., D.O. Smith, and J.B. Goodenough, *Domain-Wall Structure in Permalloy Films*. Journal of Applied Physics, 1958. **29**(3): p. 294-295.
33. Hubert, A. and R. Schäfer, *Magnetic Domains: The Analysis of Magnetic Microstructures*. 1998: Springer.
34. Hrabec, A., et al., *Velocity Enhancement by Synchronization of Magnetic Domain Walls*. Physical Review Letters, 2018. **120**(22): p. 227204.
35. O'Brien, L., et al., *Dynamic Oscillations of Coupled Domain Walls*. Physical Review Letters, 2012. **108**(18): p. 187202.
36. Parkin, S.S.P., M. Hayashi, and L. Thomas, *Magnetic domain-wall racetrack memory*. Science, 2008. **320**(5873): p. 190-194.
37. Dawidek, R.W., et al., *Dynamically-Driven Emergence in a Nanomagnetic System*. Advanced Functional Materials. **n/a**(n/a): p. 2008389.
38. Edgcombe, C.J., *A phase plate for transmission electron microscopy using the Aharonov-Bohm effect*. Journal of Physics: Conference Series, 2010. 241: p. 012005.

### Data availability:

All data associated with this manuscript are available on the XXX repository at DOI:XXXXXXXX

### Code availability Statement:

All analysis code and reconstruction algorithms associated with the work of this manuscript are available on the YYY repository at DOI:YYYY

### Extended Data Captions:

*Extended Data 1: The reconstructed x, y and z components of the magnetisation through a centre slice of the helix (a-c, respectively, with outlines indicating the helix structure) compared with the corresponding components of the magnetisation (d-f) of the micromagnetic simulation shown in g.*

### Methods:

#### 3D geometrical parameters of the cobalt double helices:

In curved three-dimensional systems, it is useful to define the geometrical properties in terms of the curvature  $\kappa$  and torsion  $\tau$  of the system, which are defined as:

$$\kappa = \frac{r_H}{r_H^2 + P^2}, \tau = \frac{CP}{r_H^2 + P^2}$$

Where  $r_H$  is the helix radius,  $P = p_H/2\pi$  with  $p_H$  the helix pitch,  $C$  is the chirality, and where the radii of curvature and torsion are defined as  $\kappa^{-1}$  and  $\tau^{-1}$ , respectively. It has been shown analytically that the radii of curvature and torsion determine the effective anisotropy, and spin wave dynamics

of a single magnetic helix [20]. The helices investigated experimentally in this work have the following geometrical parameters:

*Fabrication:*

The 3D cobalt double helices were fabricated using focused electron beam induced deposition (FEBID) combined with a CAD-software compatible program that allows for the deposition of 3D architectures. Specifically, a single pixel double helix model was designed using the opensource program FreeCAD. Following the growth of calibration structures to account for the growth rate of the cobalt precursor according to [23], a stream file to direct the scanning electron beam was created.

The double helices were fabricated on OMNI probe TEM sample holders, which were pre-milled with the focused ion beam to prevent shadowing of the sample holder during the laminography scan. Both the FIB milling and FEBID growth were performed in a Helios 660 NanoLab focused ion beam microscope at the Kelvin Nanocharacterisation Centre of the University of Glasgow. Specifically, for the growth of the 3D magnetic nanostructures, an acceleration voltage of 5 kV and a current of 86 pA were used, in combination with the precursor  $\text{Co}_2(\text{CO})_8$ . The growth times varied between 20 and 30 min per double helix structure.

Following the deposition, the samples were annealed for 40 min at 250°C, which results in an increase in the spontaneous magnetisation of the cobalt, without a significant increase of crystalline size or texture formation [42, 43]. In particular, the annealing leads to a nanocrystalline microstructure, a cobalt composition of ~80 at. % and a saturation magnetisation of 800-900 kA/m. This treatment also leads to the formation of a protective carbon shell around the surface of the three-dimensional structure. The annealing procedure has the additional advantage of reducing carbon deposition – and in turn, any deformation of the structure – during the X-ray imaging experiments.

*X-ray magnetic laminography:*

Soft X-ray magnetic laminography was performed at the PoLux beamline at the Swiss Light Source, Switzerland [10]. X-ray magnetic laminography is a recently developed 3D imaging technique which involves the measurement of projections of the magnetisation of a sample for many different orientations of the sample with respect to an X-ray beam [9].

Sensitivity to the magnetisation is obtained by probing the X-ray magnetic circular dichroism. In this measurement, the XMCD was probed at the Co  $L_2$  edge with a photon energy of 796 eV. Although the XMCD contrast at the  $L_2$  edge is weaker than the  $L_3$  edge, measurements were performed at the  $L_2$  edge due to the high absorption of the double helices, providing a balance between the transmission and magnetic contrast to optimise image quality. We note that due to the higher curvature of Helix A, the effective thickness of the nanowire probed by the X-rays is higher, leading to a lower signal to noise ratio in the image compared to Helix B under otherwise equal imaging conditions. For each orientation, XMCD images were measured by measuring STXM images with C+, C- and linear (Horizontal) polarisation. In order to obtain a quantitative measure of the projection of the magnetisation, so-called “dark field” signal originating from leakage of the centre stop of the zoneplate and from the higher order light diffracted by the monochromator was removed from the projections by applying the following normalisation procedure:

$$T = \frac{I - DF}{I_0 - DF}$$

Where  $T$  is the normalised transmitted intensity,  $I$  is the nominal transmitted intensity,  $I_0$  is the intensity incident on the sample obtained from an empty region of the image, and  $DF$  is the “dark-field” signal, that is estimated from regions of the image where the incident beam is blocked. The linear light projections were used to cross-check the removal of the unfocused and higher energy light. In this way, quantitative projections of the magnetisation were obtained, which were used to obtain a correct reconstruction of the three-dimensional magnetisation.

For the two dimensional imaging of the helices shown in Figure 1 before and after the application of a transverse magnetic field, the samples were mounted in the laminography stage, and aligned such that the X-rays were aligned with the direction of the long axis of the helix, resulting in an incident angle of the X-rays and long axis of the helix of  $45^\circ$ , providing sensitivity to the component of the magnetisation parallel to the long axis of the helix. In Figure 1, the images f,h,g,i were measured with 8, 2, 9 and 4 averages, respectively, leading to slight changes in the noise level of the individual images.

For the three-dimensional imaging, the X-ray laminography setup consisted of a rotation stage whose rotation axis is oriented at  $45^\circ$  to the X-ray beam. Projections were measured with an angular separation of  $10^\circ$ . In laminography, the number of  $N$  projections measured over  $360^\circ$  required to achieve a spatial resolution  $\Delta r$  is defined as [44]:

$$N = \pi \frac{T}{\Delta r} \tan \theta_L$$

Where  $T$  is the thickness of the sample, and  $\theta_L$  is the laminography angle, which defines the angle between the X-ray beam and the rotation axis – in this case  $45^\circ$ .

In this measurement, projections of the structure with a field of view of  $3 \times 3 \mu\text{m}^2$ , and a pixel size of 25 nm were measured around  $360^\circ$  with an angular separation of  $10^\circ$ . For each angle, an average of 2 XMCD projections was measured in order to increase the signal to noise ratio. The angular separation of  $10^\circ$  corresponds to a nominal spatial resolution  $\Delta r$  of sub-20 nm. In reality, the spatial resolution of the final reconstruction was limited by the signal to noise ratio of the XMCD projections. Of the 36 projections, it was only possible to measure 27 due to shadowing of the X-ray beam due to the sample holder. Simulations of magnetic laminography revealed that although this led to an asymmetry in the reconstructed magnetisation, it does not prevent the identification of the locked domain wall state.

The three-dimensional magnetic configuration was then reconstructed using a GPU-implementation of an arbitrary projection reconstruction algorithm developed in [28] and used in [9, 10].

The three-dimensional magnetisation structure was visualised with Paraview 5.5.0.

### *Magnetic laminography reconstruction*

The reconstructed  $m_x$ ,  $m_y$  and  $m_z$  components of the magnetic configuration are presented in **Extended Data 1a-c**, respectively, where they are directly compared to the micromagnetic simulation of the locked domain wall state in **Extended Data 1d-f**. The multidomain structure is confirmed by the  $m_x$  component, which reveals positive and negative domains on the upper and

lower halves of the helix, respectively. However, it is only with the transverse components of the magnetisation,  $m_y$  and  $m_z$ , that the type of domain wall pairs state can be identified: both the  $m_y$  and  $m_z$  components exhibit an alternating contrast (**Extended Data 1b,c**), consistent with the “locked” domain wall state (**Extended Data 1e,f**), and not with the more standard “unlocked” domain wall pair configuration previously observed in planar systems.

#### *Micromagnetic simulations:*

Finite element meshes were created by first creating STL files corresponding to three-dimensional double helices of different parameters using the open source program FreeCAD. For all simulations, the nanowire diameter was kept constant at 50 nm, while the helix radii and pitches were varied. The meshes were created with a mesh size of 5 nm using the program Gmsh [45].

To map the phase diagram of the stable state after transverse saturation of the magnetisation, micromagnetic simulations were performed using the program Magnum.fe, that employs finite-element micromagnetics with a hybrid finite-element/boundary-element method for the magnetostatic field computation and a preconditioned implicit time integration scheme for the LLG equation [46]. The spontaneous magnetisation of the material was fixed to  $M_S = 8 \times 10^5$  A/m. The magnetisation was initialised in the transverse direction, assuming full saturation, and then the relaxation calculated using the LLG equation with a damping parameter  $\alpha = 1$ .

To calculate the stray field around the final magnetisation state, the double helix mesh was embedded within a boxed mesh using the program Gmsh, and the stray field calculated at each position using the Magnum.fe solver.

In order to compare the helix configuration with that of a straight nanowire, a coordinate transformation was applied to the relaxed locked domain wall configuration result using Paraview, and the magnetisation transformed accordingly. Following the “unwinding” of the magnetic state, the configuration was once more allowed to relax using Magnum.fe in order to reach a stable configuration. The micromagnetic simulations presented in Figures 3 and 4 of the main text correspond to a Helix pitch of 500 nm, a Helix radius of 30 nm, and a nanowire diameter of 50 nm.

#### *References:*

39. Stiller, M., et al., *Functionalized Akiyama tips for magnetic force microscopy measurements*. Measurement Science and Technology, 2017. **28**(12): p. 125401.
40. Mach-Battle, R., et al., *Tailoring Magnetic Fields in Inaccessible Regions*. Physical Review Letters, 2020. **125**(17): p. 177204.
41. Gliga, S., et al., *Emergent dynamic chirality in a thermally driven artificial spin ratchet*. Nature Materials, 2017. **16**(11): p. 1106-1111.
42. Pablo-Navarro, J., C. Magén, and J.M. de Teresa, *Purified and Crystalline Three-Dimensional Electron-Beam-Induced Deposits: The Successful Case of Cobalt for High-Performance Magnetic Nanowires*. ACS Applied Nano Materials, 2018. **1**(1): p. 38-46.
43. Fernández-Pacheco, A., et al., *Writing 3D Nanomagnets Using Focused Electron Beams*. 2020. **13**(17): p. 3774.
44. Holler, M., et al., *Three-dimensional imaging of integrated circuits with macro- to nanoscale zoom*. Nature Electronics, 2019. **2**(10): p. 464-470.
45. Geuzaine, C. and J.-F. Remacle, *Gmsh: A 3-D finite element mesh generator with built-in pre- and post-processing facilities*. Numerical Methods in Engineering, 2009. **79**(11): p. 1309-1331.
46. Abert, C., *Micromagnetics and spintronics: models and numerical methods*. The European Physical Journal B, 2019. **92**(6): p. 120.

